bioRxiv preprint doi: https://doi.org/10.1101/726760; this version posted August 6, 2019. The copyright holder for this preprint (which was not certified by peer review) is the author/funder, who has granted bioRxiv a license to display the preprint in perpetuity. It is made available under aCC-BY-NC-ND 4.0 International license.

Title: Myelin and nodal plasticity modulate action potential conduction in the adult mouse brain

Authors: Carlie L Cullen[1#], Renee E Pepper[1#], Mackenzie T Clutterbuck[1], Kimberley A Pitman[1], Viola Oorschot[2], Loic Auderset[1], Alexander D Tang[3], Georg Ramm[2], Ben Emery[4], Jennifer Rodger[3,5], Renaud B Jolivet[6,7], Kaylene M Young[1*]

Affiliations:

[1] Menzies Institute for Medical Research, University of Tasmania, Hobart, AUS.

[2] Ramaciotti Centre for Cryo-Electron Microscopy, Monash University, Melbourne, AUS

[3] Experimental and Regenerative Neurosciences, School of Biological Sciences, University of Western Australia, Perth, AUS.

[4] Jungers Center for Neurosciences Research, Department of Neurology, Oregon Health and Science University, Portland, OR, USA.

[5] Perron Institute for Neurological and Translational Research, Perth, AUS.

[6] Département de Physique Nucléaire et Corpusculaire, University of Geneva, Geneva, Switzerland

[7] CERN, Geneva, Switzerland

[#]These authors contributed equally

*Correspondence to: kaylene.young@utas.edu.au

Abstract: Myelination of central nervous system axons increases action potential conduction velocity and increases the speed of information transfer. However, it is unclear whether myelination optimizes action potential conduction to achieve synchronicity and facilitate information processing within cortical and associative circuits. Here we show that myelin sheaths remain plastic in the adult mouse and undergo subtle structural modifications to influence action potential conduction. Repetitive transcranial magnetic stimulation and spatial learning, two stimuli that modify neuronal activity, alter the length of the nodes of Ranvier and the size of the periaxonal space within active brain regions. This change in the axon-glial configuration, which is independent of oligodendrogenesis, tunes conduction velocity to increase the synchronicity of action potential conduction.

One Sentence Summary: The activity-dependent modulation of nodes of Ranvier and the periaxonal space allows central conduction to be tuned to achieve synchronicity.

bioRxiv preprint doi: https://doi.org/10.1101/726760; this version posted August 6, 2019. The copyright holder for this preprint (which was not certified by peer review) is the author/funder, who has granted bioRxiv a license to display the preprint in perpetuity. It is made available under aCC-BY-NC-ND 4.0 International license.

Main Text:

Within the central nervous system (CNS), oligodendrocytes elaborate myelin internodes to facilitate the rapid and saltatory conduction of action potentials and to provide vital trophic support to axons via the periaxonal space (*1*). During development, the extension and retraction of internodes is regulated by neuronal activity and calcium signaling within the nascent myelin sheaths [reviewed in (*2*)], and after maturation, oligodendrocytes retain some capacity to lengthen or shorten their internodes (*3, 4*). However, the extent to which mature oligodendrocytes can adapt, when the pattern of neuronal activity is altered, to dynamically modulate action potential conduction has not been explored.

To determine whether increased cortical activity can induce adaptive changes in mature, myelinating oligodendrocytes, we labeled a subset of mature cortical oligodendrocytes, by giving tamoxifen to adult *Plp-CreER::Tau-mGFP* transgenic mice, one week prior to commencing non-invasive, low-intensity repetitive transcranial magnetic stimulation (rTMS) of the primary motor cortex (M1), using a specialized rodent coil (*5*). 14 days of intermittent theta burst stimulation (iTBS) did not alter the length of $mGFP^+$ internodes within M1 or the corpus callosum (CC), or influence the number of internodes supported by an individual myelinating oligodendrocyte (**Figures S1 and S2**). Overall, therefore, mature oligodendrocyte morphology was not grossly altered.

However, iTBS subtly changed myelin structure. Anchoring proteins expressed within the myelin loops of each internode interact with the axonal proteins contactin and contactin-associated protein (Caspr) to form paranodes that maintain voltage-gated sodium channels ($NaV_{1.6}$) at the nodes of Ranvier [reviewed in (*2*)]. We immunolabeled coronal brain sections to visualize the nodes of Ranvier ($NaV_{1.6}$) that were clearly flanked by two abutting paranodes (Caspr) (**Figure 1A-D**), and

bioRxiv preprint doi: https://doi.org/10.1101/726760; this version posted August 6, 2019. The copyright holder for this preprint (which was not certified by peer review) is the author/funder, who has granted bioRxiv a license to display the preprint in perpetuity. It is made available under aCC-BY-NC-ND 4.0 International license.

found that iTBS shifted the node length distribution towards shorter nodes within M1 (**Figure 1E**) and the CC (**Figure 1F**). This corresponded to a ~10% reduction in the average node length in M1 (**inset Figure 1E**), and an ~8% decrease in the CC (**Figure 1F**). 7 days after stimulation ceased, the M1 node length returned to sham levels in iTBS mice (**Figure 1G**), suggestive of bidirectional plasticity. However, within the CC the length distribution remained significantly shifted towards shorter nodes, corresponding to an ~11% decrease in average node length (**Figure 1H**).

Node lengthening occurs pathologically in response to cerebral microvascular disease (*6*) and demyelination induced by multiple sclerosis, but the nodal domains are restored at sites of remyelination (*7*). Nodal elongation has also been observed acutely following a partial optic nerve transection (*8*), and it has been reported that three days of chronic cerebral hypoperfusion is associated with a progressive lengthening of nodes, although this was accompanied by damage to the paranodal septate-like junctions (*9*). However, iTBS-induced nodal changes are unlikely to reflect a pathological response, as node length decreased (rather than increased) and no change was detected in the average length or length distribution of paranodes in M1 or the CC (**Figure S3**).

Patterns of neuronal activity can also be physiologically altered through learning, and motor learning has been shown to promote oligodendrogenesis and increase myelination of active neural circuits [reviewed in (*2*)]. To investigate this, we exposed mice to spatial learning training in the radial arm maze (**Figure S4**), to increase neuronal activity in the hippocampus, and then examined node length in the fimbria, a major output tract of the hippocampus. Spatial learning shifted the node length distribution towards longer nodes and increased average node length by ~31% (**Figure 1I-K**). This was accompanied by a small but significant ~5% increase in paranode length (**Figure**

bioRxiv preprint doi: https://doi.org/10.1101/726760; this version posted August 6, 2019. The copyright holder for this preprint (which was not certified by peer review) is the author/funder, who has granted bioRxiv a license to display the preprint in perpetuity. It is made available under aCC-BY-NC-ND 4.0 International license.

S4). These data indicate that the nodes of Ranvier are dynamic and can shortened or lengthened in response to neuronal activity.

Schneider et al. (*10*) recently demonstrated that ongoing oligodendrogenesis is required to maintain nodes at their usual length, as reducing cortical oligodendrogenesis lengthened the nodes of Ranvier. As iTBS does not alter oligodendrocyte addition in the adult mouse CC (*5*), oligodendrogenesis is unlikely to explain iTBS- or learning-induced nodal plasticity. To confirm this, we prevented adult oligodendrogenesis using *Pdgfrα-CreER^{TM}::Rosa26-YFP::Myrf$^{fl/fl}$* (*Myrf*-deleted) mice, to allow the conditional deletion of *myelin regulatory factor* (*Myrf*), a transcription factor essential for myelin production and maintenance (*11*). The conditional deletion of *Myrf* from adult oligodendrocyte progenitor cells reduced oligodendrogenesis in M1 and the CC by >60% (**Figure S5**); however, iTBS significantly shifted the node length distribution towards shorter nodes in these mice (**Figure 2A-D**), reducing node length in M1 by ~17% (**Figure 2C**) and in the CC by ~12% (**Figure 2D**). Our conclusion that node shortening during iTBS is mediated by mature and not newborn oligodendrocytes is further supported by our selective analysis of mature nodes of Ranvier. Nodes flanked by mGFP^{+} internodes in *Plp-CreER::Tau-mGFP* transgenic mice were formed prior to sham stimulation or iTBS (**Figure 2E, F**), and yet iTBS significantly shortened these mature nodes by ~16% in M1 (**Figure 2G**) and the CC (**Figure 2H**).

The sustained activation of extracellular signal-regulated kinases 1 and 2 in mature oligodendrocytes shortens nodes by increasing myelin thickness (*12*). Transmission electron microscopy revealed that the g-ratio [axon diameter / (axon + myelin sheath diameter)] of myelinated callosal axons was reduced by ~5% in iTBS mice compared to sham-stimulated mice (**Figure 3A, B**), without any change in axon diameter (iTBS: 0.53 ± 0.17µm; sham: 0.58 ± 0.16µm, t-test p=0.09). A decreased g-ratio is often interpreted as increased myelin thickness; however, by

bioRxiv preprint doi: https://doi.org/10.1101/726760; this version posted August 6, 2019. The copyright holder for this preprint (which was not certified by peer review) is the author/funder, who has granted bioRxiv a license to display the preprint in perpetuity. It is made available under aCC-BY-NC-ND 4.0 International license.

counting the major dense lines within each myelin sheath, we found that the number of myelin wraps was not affected by treatment (**Figure 3C-G**), and neither the thickness of each wrap (**Figure 3H**), nor the width of the inner tongue process (sham: 30.46 ± 2.31nm; iTBS: 32.14 ± 2.38nm, Mann-Whitney U test p=0.4) changed in response to iTBS treatment. Surprisingly, iTBS increased the width of the space between the axon and the myelin sheath, known as the periaxonal space, by ~31% (**Figure 3I**).

This is the first report of an ultrastructural adaptation of the periaxonal space in response to altered neuronal activity. The periaxonal space has been hypothesized to act as a receptacle for calcium, glutamate and potassium released by the axon during action potential propagation, as well as oligodendrocyte-derived lactate, which is then shuttled through the monocarboxylate transporter 2 to provide metabolic support to the axon [reviewed in (*13*)]. Periaxonal space ultrastructure is altered in mice deficient in myelin-associated glycoprotein (MAG), a protein expressed specifically in the periaxonal myelin membrane [reviewed in (*14*)], and vacuoles form within this space along optic nerve axons following connexin 32 / 47 knock-out, a phenotype largely attributed to impaired potassium buffering by oligodendrocytes (*15*). A marked swelling of the periaxonal space also follows acute ischemic white matter injury and demyelination (*16*). However, vacuolization, or an uneven separation of myelin from axons, was not observed in our tissue, suggesting that the iTBS-induced expansion of the periaxonal space was not pathological, but a physiological adaptation to increased neuronal activity.

Spatial learning was also associated with periaxonal plasticity in the fimbria (**Figure 3**), inducing a small but significant ~5.8% increase in the g-ratio of myelinated axons (**Figure 3J, K**) that was not explained by a change in axon diameter (learning: 0.56 ± 0.01µm, no-learning: 0.59 ± 0.01µm, mean ± SEM; Mann Whitney-U test p=0.14) or myelin wrap number (**Figure 3L**), but which

bioRxiv preprint doi: https://doi.org/10.1101/726760; this version posted August 6, 2019. The copyright holder for this preprint (which was not certified by peer review) is the author/funder, who has granted bioRxiv a license to display the preprint in perpetuity. It is made available under aCC-BY-NC-ND 4.0 International license.

corresponded to an ~19% decrease in periaxonal space width (**Figure 3M-O**). These data suggest that a single bidirectional mechanism links changes in neuronal activity with a change in myelin structure: iTBS was associated with a contraction of the nodes of Ranvier and an expansion of the periaxonal space for axons in the CC, whereas spatial learning was associated with an extension of the nodes of Ranvier and a contraction of the periaxonal space in the fimbria.

Alterations to both the periaxonal space (*17, 18*) and nodal domains (*10, 19, 20*) are predicted to exert a strong influence on conduction speed and may therefore impact the timing of action potentials, which is crucial for effective information processing. To determine how iTBS-induced changes in node length and periaxonal ultrastructure influence conduction speed, we performed computational simulations of action potential propagation in myelinated callosal axons by adapting the mathematical model developed by Richardson and colleagues (*21*; see supplementary methods and **Figures S6** and **S7**). First, we used a parameter set matching the observations obtained in the sham condition (**Table S1**), which resulted in a theoretical conduction velocity of 1.18m/s. Reducing the node length by 8%, as occurred during iTBS (**Figure 1**), slowed action potential propagation by ~2.3%, whereas altering the myelin sheath parameters (decreased g-ratio + increased periaxonal space; **Figure 3**) exerted a greater effect on conduction speed, effectively slowing propagation by ~8.7% (**Figure 4A, B**). Finally, a fourth simulation implementing all ultrastructural changes observed following iTBS (reduced node length and g-ratio + increased periaxonal space) produced an additive effect, slowing conduction by ~10.9% (1.05m/s; **Figure 4B**).

Consistent with our simulation data, *ex vivo* field potential recordings of compound action potentials (CAPs) in the CC revealed that myelinated axon conduction velocity was 1.27 ± 0.19 m/s under sham conditions and slowed by ~18% following iTBS (1.04 ± 0.19 m/s; **Figure 4C, D**).

bioRxiv preprint doi: https://doi.org/10.1101/726760; this version posted August 6, 2019. The copyright holder for this preprint (which was not certified by peer review) is the author/funder, who has granted bioRxiv a license to display the preprint in perpetuity. It is made available under aCC-BY-NC-ND 4.0 International license.

In addition, the amplitude of the myelinated axon CAP increased by ~40% following iTBS (**Figure 4E**), and its half-width decreased by ~9% (**Figure 4F**), suggesting that a greater number of action potentials arrived simultaneously at the recording electrode. The unmyelinated axon component of the CAP was not altered by iTBS (**Figure 4C-F**). These data suggest that, in response to altered neuronal activity, oligodendrocytes make subtle changes to myelin ultrastructure that impact the length of nodes of Ranvier and the size of the periaxonal space, and fine-tune conduction velocity to increase the synchronicity of action potentials within the active circuit. In this way, mature, myelinating oligodendrocytes may contribute to the dynamic regulation of information processing in the central nervous system that ensures the ongoing adaptability of the neural network throughout life.

References

1. M. Simons, K. A. Nave, Oligodendrocytes: Myelination and Axonal Support. *Cold Spring Harb Perspect Biol* **8**, a020479 (2015).
2. R. E. Pepper, K. A. Pitman, C. L. Cullen, K. M. Young, How do cells of the oligodendrocyte lineage affect neuronal circuits to influence motor function, memory and mood? *Frontiers in cellular neuroscience* **12**, (2018).
3. R. A. Hill, A. M. Li, J. Grutzendler, Lifelong cortical myelin plasticity and age-related degeneration in the live mammalian brain. *Nature Neuroscience* **21**, 683-695 (2018).
4. F. Auer, S. Vagionitis, T. Czopka, Evidence for Myelin Sheath Remodeling in the CNS Revealed by In Vivo Imaging. *Current Biology* **28**, 549-559.e543 (2018).
5. C. L. Cullen *et al.*, Low-intensity transcranial magnetic stimulation promotes the survival and maturation of newborn oligodendrocytes in the adult mouse brain. *Glia* **67**, 1462-1477 (2019).
6. J. D. Hinman, M. D. Lee, S. Tung, H. V. Vinters, S. T. Carmichael, Molecular disorganization of axons adjacent to human lacunar infarcts. *Brain* **138**, 736-745 (2015).
7. O. Howell *et al.*, Disruption of neurofascin localization reveals early changes preceding demyelination and remyelination in multiple sclerosis. *Brain* **129**, 3173-3185 (2006).
8. R. L. O'Hare Doig *et al.*, Specific ion channels contribute to key elements of pathology during secondary degeneration following neurotrauma. *BMC neuroscience* **18**, 62 (2017).
9. M. Reimer *et al.*, Rapid disruption of axon-glial integrity in response to mild cerebral hypofusion. *The Journal of neuroscience* **31**, 18185-18194 (2011).
10. S. Schneider *et al.*, Decrease in newly generated oligodendrocytes leads to motor dysfunctions and changed myelin structures that can be rescued by transplanted cells. *Glia* **64**, 2201-2218 (2016).
11. B. Emery *et al.*, Myelin gene regulatory factor is a critical transcriptional regulator required for CNS myelination. *Cell* **138**, 172-185 (2009).

bioRxiv preprint doi: https://doi.org/10.1101/726760; this version posted August 6, 2019. The copyright holder for this preprint (which was not certified by peer review) is the author/funder, who has granted bioRxiv a license to display the preprint in perpetuity. It is made available under aCC-BY-NC-ND 4.0 International license.

12. M. A. Jeffries *et al.*, ERK1/2 Activation in Preexisting Oligodendrocytes of Adult Mice Drives New Myelin Synthesis and Enhanced CNS Function. *The Journal of Neuroscience* **36**, 9186-9200 (2016).
13. I. Micu, J. R. Plemel, A. V. Caprariello, K.-A. Nave, P. K. Stys, Axo-myelinic neurotransmission: a novel mode of cell signalling in the central nervous system. *Nature Reviews Neuroscience* **19**, 49 (2017).
14. R. H. Quarles, Myelin-associated glycoprotein (MAG): past, present and beyond. *Journal of neurochemistry* **100**, 1431-1448 (2007).
15. D. M. Menichella *et al.*, Genetic and Physiological Evidence That Oligodendrocyte Gap Junctions Contribute to Spatial Buffering of Potassium Released during Neuronal Activity. *The Journal of Neuroscience* **26**, 10984-10991 (2006).
16. F. Aboul-Enein *et al.*, Preferential Loss of Myelin-Associated Glycoprotein Reflects Hypoxia-Like White Matter Damage in Stroke and Inflammatory Brain Diseases. *Journal of Neuropathology & Experimental Neurology* **62**, 25-33 (2003).
17. J. A. Halter, J. W. Clark, Jr., The influence of nodal constriction on conduction velocity in myelinated nerve fibers. *Neuroreport* **4**, 89-92 (1993).
18. K. M. Young *et al.*, Oligodendrocyte dynamics in the healthy adult CNS: evidence for myelin remodeling. *Neuron* **77**, 873-885 (2013).
19. M. Ford *et al.*, Tuning of Ranvier node and internode properties in myelinated axons to adjust action potential timing. *Nature communications* **6**, 8073 (2015).
20. I. L. Arancibia-Carcamo *et al.*, Node of Ranvier length as a potential regulator of myelinated axon conduction speed. *eLife* **6**, e23329 (2017).
21. A. G. Richardson, C. C. McIntyre, W. M. Grill, Modelling the effects of electric fields on nerve fibres: Influence of the myelin sheath. *Medical and Biological Enginerring and Computing* **38**, 438-446 (2000).
22. N. H. Doerflinger, W. B. Macklin, B. Popko, Inducible site-specific recombination in myelinating cells. *genesis* **35**, 63-72 (2003).
23. S. H. Kang, M. Fukaya, J. K. Yang, J. D. Rothstein, D. E. Bergles, NG2+ CNS glial progenitors remain committed to the oligodendrocyte lineage in postnatal life and following neurodegeneration. *Neuron* **68**, 668-681 (2010).
24. Y. Bakiri, R. Káradóttir, L. Cossell, D. Attwell, Morphological and electrical properties of oligodendrocytes in the white matter of the corpus callosum and cerebellum. *The Journal of Physiology* **589**, 559-573 (2011).
25. C. C. McIntyre, W. M. Grill, Extracellular Stimulation of Central Neurons: Influence of Stimulus Waveform and Frequency on Neuronal Output. *Journal of Neurophysiology* **88**, 1592-1604 (2002).
26. D. K. Crawford, M. Mangiardi, S. K. Tiwari-Woodruff, Assaying the functional effects of demyelination and remyelination: revisiting field potential recordings. *Journal of neuroscience methods* **182**, 25-33 (2009).
27. G. David, B. Modney, K. A. Scappaticci, J. N. Barrett, E. F. Barrett, Electrical and morphological factors influencing the depolarizing after-potential in rat and lizard myelinated axons. *The Journal of Physiology* **489**, 141-157 (1995).

Acknowledgments: We thank our colleagues at the University of Tasmania and Rowan Tweedale (Queensland Brain Institute, the University of Queensland) for constructive feedback and suggestions for improvement. We also thank Dr Lee Cossell for his advice on computational

bioRxiv preprint doi: https://doi.org/10.1101/726760; this version posted August 6, 2019. The copyright holder for this preprint (which was not certified by peer review) is the author/funder, who has granted bioRxiv a license to display the preprint in perpetuity. It is made available under aCC-BY-NC-ND 4.0 International license.

modelling. **Funding:** This research was supported by grants from the National Health and Medical Research Council of Australia (NHMRC; 1077792, 1139041), MS Research Australia (11-014, 16-105; 17-007), the Australian Research Council (DP180101494), the Swiss National Science Foundation (31003A_170079) and the National MS Society. CLC was supported by a fellowship from MS Research Australia and the Penn Foundation (15-054). KAP was supported by a fellowship from the NHMRC (1139180). LA was supported by an Australian Postgraduate Award. MTC and RP were supported by scholarships from the Menzies Institute for Medical Research. BE was supported a fellowship from the NHMRC (1032833) and a Warren endowed professorship in neuroscience research. KMY was supported by fellowships from the NHMRC (1045240) and MS Research Australia / the Macquarie Group Foundation (17-0223). JR was supported by fellowships from the NHMRC (1002258) and the Perron Institute for Neurological and Translational Science and MS Western Australia. **Author contributions:** CLC, KMY, REP, KAP, JR and RBJ developed the project and wrote the manuscript. CLC, REP, KAP, MTC, LA, VO, RBJ and KMY carried out the experiments. KMY, JR, CLC, BE and RBJ obtained the funding. CLC, REP, MTC and RBJ performed the statistical analyses and generated the figures. KMY, ADT, GR, JR and CLC provided supervision. **Competing interests:** Authors declare no competing interests. **Data and materials availability:** The use of all transgenic mouse lines complies with the conditions of their materials transfer agreements. All data are available in the main text or the supplementary materials.

Supplementary Materials:

Materials and Methods

Figures S1-S5

Tables S1

References (*22-27*)

bioRxiv preprint doi: https://doi.org/10.1101/726760; this version posted August 6, 2019. The copyright holder for this preprint (which was not certified by peer review) is the author/funder, who has granted bioRxiv a license to display the preprint in perpetuity. It is made available under aCC-BY-NC-ND 4.0 International license.

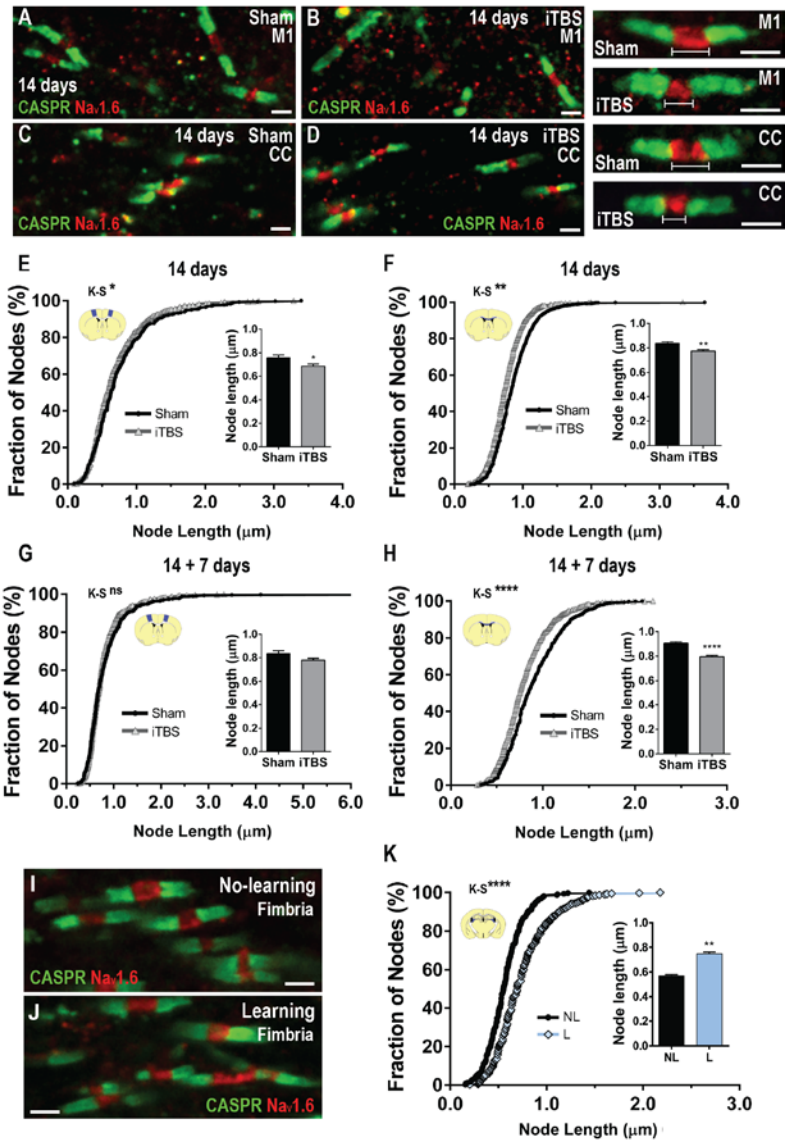

Figure 1. iTBS and spatial learning modulate node length.
(**A-D**) Confocal images of nodes of Ranvier (NaV1.6; red) and paranodes (CASPR; green) in M1 (**A, B**) and the CC (**C, D**) after 14 day of sham-stimulation or iTBS. (**E-F**) Node length distribution in M1 (**E**; 400 sham and 538 iTBS nodes; K-S D=0.097, p=0.02; inset, average node length, Mann Whitney U (MWU) test, p=0.01) and CC [**F**; 667 sham and 507 iTBS nodes; Kolmogorov-Smirnov (K-S) D=0.13, p=0.0001; inset, average node length, MWU test, p=0.006] of mice receiving sham-stimulation (black bars) or iTBS (gray bars). (**G-H**) Node length distribution in M1 (**G**; 452 sham and 576 iTBS nodes; K-S D=0.070, p=0.15; inset, average node length, MWU test, p=0.35) and CC (**H**; 587 sham and 696 iTBS nodes; K-S D=0.16, p<0.0001; inset, average node length, MWU test, p<0.0001) of mice 7 days after cessation of sham-stimulation (black bars) and iTBS (gray bars) (14 + 7 days). (**I-J**) Confocal images of nodes of Ranvier and paranodes in the hippocampal fimbria after 14 days no-learning (NL; **I**) or learning (L; **J**). (**K**) Node length distribution in the fimbria (310 NL and 379 L nodes; K-S D=0.307, p<0.0001; inset, average node length, MWU test, p<0.0001) of NL (black bars) and L (blue bars) mice. * p<0.05, ** p<0.01, ****p<0.0001. Mean ± SEM. Scale bars represent 1µm.

bioRxiv preprint doi: https://doi.org/10.1101/726760; this version posted August 6, 2019. The copyright holder for this preprint (which was not certified by peer review) is the author/funder, who has granted bioRxiv a license to display the preprint in perpetuity. It is made available under aCC-BY-NC-ND 4.0 International license.

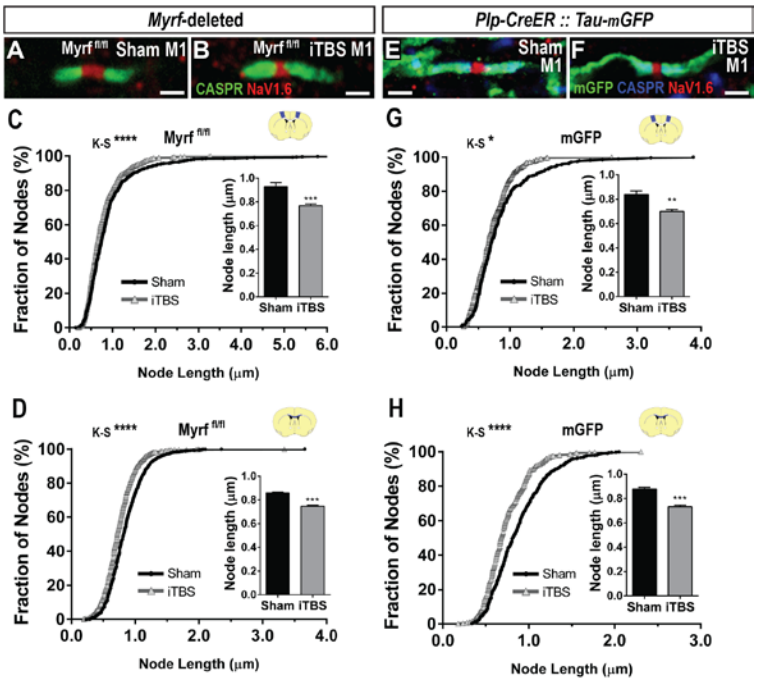

Figure 2. Mature oligodendrocytes mediate activity-dependent changes in node of Ranvier length (**A-B**) Node of Ranvier ($NaV_{1.6}$; red) in M1 of *Myrf*-deleted mice (*Pdgfrα-CreER*^{TM}*::Myrf*$^{fl/fl}$) after 14 days of sham-stimulation (**A**) or iTBS (**B**). (**C-D**) Node length distribution in M1 [**C**; 620 sham and 727 iTBS nodes; Kolmogorov-Smirnov (K-S) D=0.12, p<0.0001; inset average node length, Mann Whitney U (MWU) test, p<0.0001] and CC (**D**; 1650 sham and 1234 iTBS nodes; K-S D=0.17, p<0.0001; inset average node length, MWU test, p<0.0001) of of *Myrf*-deleted mice after 14 days of sham-stimulation (black) or iTBS (gray). (**E-F**) Mature node of Ranvier flanked by $CASPR^+$ paranodes (blue) and $mGFP^+$ internodes (green) in M1 of *Plp-CreER::Tau-mGFP* mice, formed prior to sham-stimulation (**E**) or iTBS (**F**). (**G-H**) Mature node length distribution in M1 (**G**; 273 sham and 325 iTBS mature nodes; K-S D=0.11, p=0.03; inset, average node length, MWU test, p=0.0019) and the CC (**H**; 495 sham and 435 iTBS mature nodes; K-S D=0.22, p<0.0001; inset, average node length, MWU test, p<0.0001) of sham-stimulated (black) and iTBS (gray) mice. *p<0.05, ** p<0.01, *** p<0.001, **** p<0.0001. Mean ± SEM. Scale bars represent 1μm.

bioRxiv preprint doi: https://doi.org/10.1101/726760; this version posted August 6, 2019. The copyright holder for this preprint (which was not certified by peer review) is the author/funder, who has granted bioRxiv a license to display the preprint in perpetuity. It is made available under aCC-BY-NC-ND 4.0 International license.

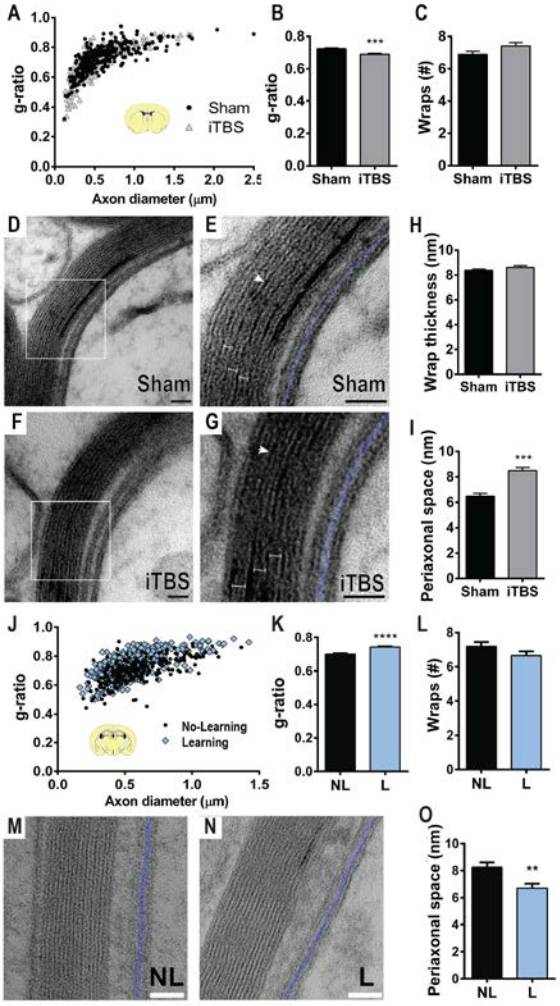

Figure 3. iTBS and spatial learning alter the size of the periaxonal space

(**A**) Axonal diameter versus g-ratio for axons in the CC of sham-stimulated (black dots; n=323) and iTBS (gray triangles; n=301) mice (Kolmogorov-Smirnov (K-S) test for g-ratio D=0.18, p<0.0001). (**B**) Average g-ratio (323 sham and 301 iTBS axons; Mann Whitney U (MWU) test p<0.0001). (**C**) Average number of myelin wraps per axon (104 sham and 125 iTBS axons; MWU test p=0.23). (**D-G**) Transmission electron microscopy images of a myelinated axon in the CC of sham-stimulated (**D, E**) and iTBS (**F, G**) mice. (**H**) Average thickness of an individual myelin wrap (75 sham and 60 iTBS axons, MWU test p=0.63. (**I**) Average width of the periaxonal space (75 sham and 60 iTBS axons, MWU test p<0.0001). (**J**) Axon diameter versus g-ratio for axons in the fimbria of no-learning (NL; black dots) or learning (L; blue diamonds) mice (209 NL and 374 L axons; K-S test for g-ratio, K-S D=0.24, p<0.0001). (**K**) Average g-ratio [209 NL axons (black bars) and 374 L axons (blue bars); MWU test, p<0.0001). (**L**) Average number of myelin wraps per axon (55 NL and 55 L axons; MWU test, p=0.10). (**M-N**) TEM images of myelinated axon in the fimbria of NL and L mice. (**O**) Average width of periaxonal space (36 NL and 38 L axons; MWU test, p=0.0023). White arrows = major dense line. Blue = periaxonal space. Capped lines = single myelin wrap. ** p<0.01, *** p<0.001, **** p<0.0001. Mean ± SEM. Scale bars = 25nm (D-G) or 50nm (M-N).

bioRxiv preprint doi: https://doi.org/10.1101/726760; this version posted August 6, 2019. The copyright holder for this preprint (which was not certified by peer review) is the author/funder, who has granted bioRxiv a license to display the preprint in perpetuity. It is made available under aCC-BY-NC-ND 4.0 International license.

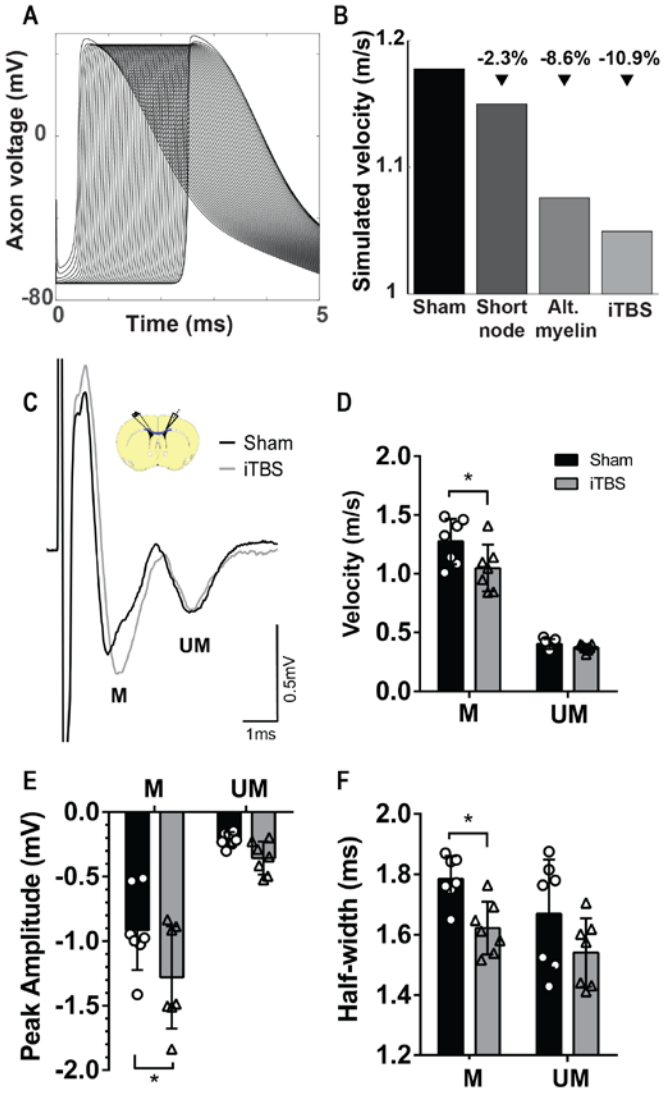

Figure 4. Increasing the size of the periaxonal space slows conduction velocity

(**A**) Action potentials simulated at consecutive nodes at 21°C. (**B**) Predicted conduction velocity of a sham-stimulated (black) axon versus an axon with either the node length or periaxonal space altered by iTBS and an axon with both node length and periaxonal space altered by iTBS. (**C**) Compound action potential (CAP) recorded in the CC of sham-stimulation (black) or iTBS (gray) mice. (**D**) Conduction velocity of myelinated (M) and unmyelinated (UM) axons in sham-stimulated (black bars, open circles) or iTBS (gray bars, open triangles) mice [2-way ANOVA: interaction $F(1,24)=3.37$, $p=0.078$; axon population $F(1,24)=211.1$, $p<0.0001$; treatment $F(1,24)=5.81$, $p=0.023$]. (**E**) Peak amplitude of M and UM axons [2-way ANOVA: interaction $F(1,24)=1.25$, $p=0.27$; axon population $F(1,24)=68.10$, $p<0.0001$; treatment $F(1,24)=6.75$, $p=0.015$]. (**F**) Half-width of CAP peak corresponding to M and UM axons [2-way ANOVA: interaction $F(1,24)=0.13$, $p=0.71$; axon population $F(1,24)=4.63$, $p=0.04$; treatment $F(1,24)=10.22$, $p=0.003$]. Mean ± SEM. * $p<0.05$ by Bonferroni's post-test.

bioRxiv preprint doi: https://doi.org/10.1101/726760; this version posted August 6, 2019. The copyright holder for this preprint (which was not certified by peer review) is the author/funder, who has granted bioRxiv a license to display the preprint in perpetuity. It is made available under aCC-BY-NC-ND 4.0 International license.

Supplementary Materials for

Myelin and nodal plasticity modulate action potential conduction in the adult mouse brain

Carlie L Cullen, Renee E Pepper, Mackenzie T Clutterbuck, Kimberley A Pitman, Viola Oorschot, Loic Auderset, Alexander D Tang, Georg Ramm, Ben Emery, Jennifer Rodger, Renaud B Jolivet, Kaylene M Young

Correspondence to: kaylene.young@utas.edu.au

This includes:

Materials and Methods
Supplementary Text
Figs. S1 to S7
Tables S1

bioRxiv preprint doi: https://doi.org/10.1101/726760; this version posted August 6, 2019. The copyright holder for this preprint (which was not certified by peer review) is the author/funder, who has granted bioRxiv a license to display the preprint in perpetuity. It is made available under aCC-BY-NC-ND 4.0 International license.

Materials and Methods

Animal housing

Male and female mice were housed in same sex groups, in individually ventilated cages (12 h light cycle, 21°C) with *ad libitum* access to food and water. Mice were randomly assigned to each treatment, but care was taken to ensure littermates were represented across treatment groups. All animal experiments were approved by the University of Tasmania Animal Ethics Committee and carried out in accordance with the Australian code of practice for the care and use of animals for scientific purposes.

Transgenic lineage tracing and gene deletion

Heterozygous *Plp-CreER* transgenic mice (22) were crossed with heterozygous *Tau-lox-STOP-lox-mGFP-IRES-NLS-LacZ-pA* (*Tau-mGFP*) Cre-sensitive reporter mice to generate double heterozygous offspring for the fluorescent labeling and tracing of oligodendrocytes. Homozygous *Myrf* loxP-flanked exon 8 mice (*Myrf* $^{fl/fl}$; 11) were crossed with heterozygous *Pdgfra-CreER*^{TM} transgenic mice (23) or homozygous *Rosa26-YFP Cre*-sensitive reporter mice to produce *Pdgfra-CreER*^{TM} *:: Myrf* $^{fl/fl}$ and *Myrf* $^{fl/fl}$ *:: Rosa26-YFP* offspring, respectively. These offspring were then intercrossed to generate *Pdgfra-CreER*^{TM} *:: Rosa26-YFP :: Myrf* $^{fl/fl}$ (*Myrf*-deleted) and *Rosa26-YFP :: Myrf* $^{fl/fl}$ (control) mice for experiments.

Cre, *Rosa26-YFP* and *Tau-mGFP* transgenes were detected by PCR as described by Cullen et al. (5), with the *Myrf* ^{floxed} gene being detected as described by Emery et al. (11). In brief, genomic DNA was extracted from ear biopsies by ethanol precipitation and PCR was performed using 50-100ng of gDNA with the following primer combinations: Cre 5’ CAGGT CTCAG GAGCT

bioRxiv preprint doi: https://doi.org/10.1101/726760; this version posted August 6, 2019. The copyright holder for this preprint (which was not certified by peer review) is the author/funder, who has granted bioRxiv a license to display the preprint in perpetuity. It is made available under aCC-BY-NC-ND 4.0 International license.

ATGTC CAATT TACTG ACCGTA and Cre 3' GGTGT TATAAG CAATCC CCAGAA; GFP 5' CCCTG AAGTTC ATCTG CACCAC and GFP 3' TTCTC GTTGG GGTCT TTGCTC; Rosa26 wildtype 5' AAAGT CGCTC TGAGT TGTTAT, Rosa26 wildtype 3' GGAGC GGGAG AAATG GATATG and Rosa26 YFP 5' GCGAA GAGTT TGTCC TCAACC; Myrf 5' AGGAG TGTTG TGGGA AGTGG and Myrf 3' CCCAG GCTGA AGATG GAATA.

To activate Cre-recombinase in oligodendrocyte precursor cells and induce targeted DNA recombination, Tamoxifen was dissolved in corn oil (40mg/ml) by sonication at 21°C for 2 h and administered to adult mice (P83) by oral gavage at a dose of 300mg tamoxifen/kg body weight daily for four consecutive days. *Plp-CreER :: Tau-mGFP* mice were given a single dose of 100mg/kg or 300mg/kg body weight to enable clear visualization of individual $mGFP^{+}$ mature oligodendrocytes following recombination (**Figure S2**).

Low intensity repetitive transcranial magnetic stimulation

Low intensity repetitive transcranial magnetic stimulation was delivered as 600 pulses of intermittent theta burst stimulation (iTBS; 192s) using a custom made 120mT circular coil designed for rodent stimulation (8mm outer diameter, iron core) as per Cullen et al. (5). Stimulation parameters were controlled by a waveform generator (Agilent Technologies) connected to a bipolar voltage programmable power supply (KEPCO BOP 100-4M, TMG test equipment). Experiments were conducted at 100% maximum power output (100V) using custom monophasic waveforms (400µs rise time; Agilent Benchlink Waveform Builder). Mice were restrained using plastic body-contour shape restraint cones (0.5mm thick; Able Scientific). The coil was manually held over the midline of the head with the back of the coil positioned in line with the front of the ears (~Bregma -3.0). Sham mice were positioned under the coil for 192s (as

bioRxiv preprint doi: https://doi.org/10.1101/726760; this version posted August 6, 2019. The copyright holder for this preprint (which was not certified by peer review) is the author/funder, who has granted bioRxiv a license to display the preprint in perpetuity. It is made available under aCC-BY-NC-ND 4.0 International license.

per iTBS), but no current was passed through the coil. Stimulation was carried out once daily, at the same time, for 14 days. LI-rTMS did not elicit observable behavioral changes in the mice during or immediately after stimulation.

Spatial learning

To induce spatial learning, adult (P60) male and female C57BL/6J mice were trained in an 8-arm radial arm maze (RAM) task (**Figure S4**) over 14 days. Beginning 5 days prior to RAM training, non-learning and learning mice were given food rewards (Froot Loops® pieces) in their home cage, with their access to normal mouse chow being restricted to 8h per day. This food restriction protocol ensured that mice were maintained at ~90% of their free feeding body weight and were motivated to seek out and consume the food rewards when available.

The RAM was carried out using the multi-maze system for mice (Ugo-Basile) in a radial 8-arm configuration. RAM training consisted of two phases - a familiarization phase (days 1-3) and a learning phase (days 4-14) (**Figure S4**), and each mouse underwent 3 trials per day, with 30 min between each trial. During the familiarization phase, all arms of the RAM were closed off and an individual mouse was placed in the octagonal center of the maze with a single Froot Loop® (cut into 8 uniformly sized pieces). The mouse remained in the center until all food rewards had been consumed, or 5 min had passed. No-learning control mice were exposed to the familiarization phase for the 14 days of the task, to ensure that they were subjected to the same environment and an equivalent level of handling and that they also received Froot Loops®, but they did not learn in the RAM (**Figure S4A**). Learning mice proceeded to undertake a learning phase, in which the 8 pieces of Froot Loop® were distributed, so that one piece was placed at the end of each arm of the RAM. An individual mouse was placed in the center of the maze with the arm-doors closed. After

bioRxiv preprint doi: https://doi.org/10.1101/726760; this version posted August 6, 2019. The copyright holder for this preprint (which was not certified by peer review) is the author/funder, who has granted bioRxiv a license to display the preprint in perpetuity. It is made available under aCC-BY-NC-ND 4.0 International license.

2 min, the doors simultaneously opened and the mouse could explore the maze until all food rewards were consumed, or 10 min had passed (**Figure S4B**). Over the next 11 days, the mice learned that each arm contained a single food reward and that repeat entries would not result in another reward. Therefore, repeated entries into an arm in which the food reward had already been consumed was counted as an error, and the average number of errors made per trial was quantified as a measure of learning (**Figure S4C**).

Tissue preparation and immunohistochemistry

Mice were perfusion-fixed with 4% paraformaldehyde (PFA; Sigma) (w/v) in phosphate buffered saline (PBS). Brains were cut into 2mm-thick coronal slices using a 1mm brain matrix (Kent Scientific) before being post-fixed in 4% PFA at 21°C for 90 min. Tissue was cryoprotected overnight in 20% (w/v) sucrose (Sigma) in PBS and snap frozen in OCT (ThermoFisher) for storage at -80°C. 30µm coronal brain cryosections were collected and processed as floating sections (as per 5). Primary and secondary antibodies were diluted in PBS blocking solution [0.1% (v/v) Triton X-100 and 10% fetal calf serum in PBS] and applied to sections overnight at 4°C, unless staining involved the use of mouse anti-CC1 (1:100 Calbiochem), in which case antibodies were diluted in Tris buffered saline (TBS) blocking solution [0.1% (v/v) Triton X-100 and 10% fetal calf serum in TBS]. Primary antibodies included goat anti-PDGFRα (1:200; GeneTex,), rabbit anti-OLIG2 (1:400 Millipore), rat anti-GFP (1:2000; Nacalai Tesque), rabbit anti-$NaV_{1.6}$ (1:500 Alomone Labs), mouse anti-CASPR (Clone K65/35; 1:200 NeuroMab). Secondary antibodies, which were conjugated to AlexaFluor -488, -568 or -647 (Invitrogen) were donkey anti-goat (1:1000), donkey anti-rabbit (1:1000), donkey anti-mouse (1:1000), and donkey anti-rat (1:500). Nuclei were labeled using Hoechst 33342 (1:1000; Invitrogen).

bioRxiv preprint doi: https://doi.org/10.1101/726760; this version posted August 6, 2019. The copyright holder for this preprint (which was not certified by peer review) is the author/funder, who has granted bioRxiv a license to display the preprint in perpetuity. It is made available under aCC-BY-NC-ND 4.0 International license.

Confocal microscopy and cell quantification

Confocal images were collected using an UltraView Nikon Ti Microscope with Volocity Software (Perkin Elmer). High magnification images (z spacing of 0.5- 2µm) were collected using standard excitation and emission filters for DAPI, FITC (AlexaFluor-488), TRITC (AlexaFluor-568) and CY5 (AlexaFluor-647), then stitched together to make a composite image of a defined region of interest. To quantify internode number and length for oligodendrocytes within the primary motor cortex (M1), high magnification images (40x objective) were collected through individual mGFP-labeled cortical oligodendrocytes (0.5µm steps) that had a visible cell body. To quantify internodes in the corpus callosum (CC), high magnification images (60x objective) were collected (0.5µm z-steps) through individual mGFP-labeled internodes capped at either end by a $CASPR^{+}$ paranode. To measure node of Ranvier ($NaV_{1.6}$) and paranode (CASPR) length, high magnification (100x) single z-plane confocal images were collected from M1, the CC and the hippocampal fimbria. Node and paranode lengths were only measured when a node and its flanking paranodes were intact within the single z-plane. For quantification of cell number, low magnification (20x objective) confocal z-stacks (2 µm spacing) were collected through M1 and the CC and stitched together to make a composite image of a defined region of interest. All image analysis was carried out using Image J (NIH) by a researcher blind to the treatment groups.

Transmission electron microscopy

Following 14 days of iTBS, sham stimulation or RAM training mice (P105 or P74) were perfused with Karnovsky's fixative (2.5% glutaraldehyde, 2% PFA, 0.25mM $CaCl_2$, 0.5mM $MgCl_2$ in 0.1M sodium cacodylate buffer). Brains were cut into 2mm-thick coronal slices using a 1mm brain matrix (Kent Scientific) and post-fixed in Karnovsky's fixative for 2 h at 21°C. The tissue blocks

bioRxiv preprint doi: https://doi.org/10.1101/726760; this version posted August 6, 2019. The copyright holder for this preprint (which was not certified by peer review) is the author/funder, who has granted bioRxiv a license to display the preprint in perpetuity. It is made available under aCC-BY-NC-ND 4.0 International license.

were rinsed and stored in 0.1M sodium cacodylate buffer overnight. The CC and hippocampal fimbria were dissected and incubated in 1% osmium tetroxide / 1.5% potassium ferricyanide [OsO_4 / $K_3Fe(III)(CN)_6$] in 0.1M sodium cacodylate buffer in the dark for 2 h at 4°C, before being dehydrated in ethanol and propylene oxide, and embedded in Epon812 resin. Ultrathin 70nm sections were cut using a Leica Ultra-cut UCT7 and stained with uranyl acetate and lead citrate. High resolution electron microscopy imaging was done at 80kV on a JEOL 1400-Flash transmission electron microscope (CC) or a Hitachi HT7700 transmission electron microscope (fimbria). Sectioning, imaging and image analysis was carried out by an experimenter blind to the treatment group.

Image analysis was carried out using Image J (NIH). The proportion of myelinated axons and g-ratio [axon diameter / (axon + myelin diameter)] were measured from at least 100 axons from 5 images per animal. The number of myelin wraps was quantified by counting major dense lines for a minimum of 15 transected axons per mouse, from n=3 mice per treatment group. The average thickness of myelin wraps per axon, the width of the adaxonal inner tongue membrane and the width of the periaxonal space were measured from axons ensheathed by myelin that was a minimum of five wraps thick (≥10 transected axons per mouse, from n=3 mice per treatment group).

Mathematical modeling

In order to evaluate the effect on action potential propagation of experimentally observed microscopic changes in node length and myelin structure (data from **Figures S1**, **1** and **3**), we adapted the mathematical model of action potential propagation in myelinated axons proposed by Richardson and colleagues (model 'C', their Fig. 1; 21). A recent MATLAB (The MathWorks)

bioRxiv preprint doi: https://doi.org/10.1101/726760; this version posted August 6, 2019. The copyright holder for this preprint (which was not certified by peer review) is the author/funder, who has granted bioRxiv a license to display the preprint in perpetuity. It is made available under aCC-BY-NC-ND 4.0 International license.

implementation of that model by Cossell and colleagues can be downloaded from GitHub (https://github.com/AttwellLab/MyelinatedAxonModel) (18-20, 24). That package was downloaded in June 2018 and run on MATLAB R2016b.

The mathematical description of ion channels at nodes of Ranvier follows the Hodgkin-Huxley formalism. Briefly, nodes express three types of ion channels, a fast sodium channel i_{Na}^{fast} responsible for the initiation of action potentials, a persistent sodium channel $i_{Na}^{\text{persistent}}$, and a slow potassium channel i_{K}^{slow} responsible for the termination of action potentials. The kinetics of the three currents is derived from McIntyre *et al.* (25). Briefly, i_{Na}^{fast} is written:

$$i_{Na}^{\text{fast}} = g_{Naf}\, m^3\, h\, (V - E_{Na}) \tag{1}$$

with g_{Naf} the current conductance, V the membrane voltage at the node, $E_{Na} = 60\text{mV}$ the reversal potential for sodium ions, and m and h some gating variables. Following the Hodgkin-Huxley formalism, each gating variable x in the model follows the generic equation:

$$\frac{dx}{dt} = \alpha_x(1 - x) - \beta_x x \tag{2}$$

with α and β some functions of V. For i_{Na}^{fast}, α and β are given by:

$$\alpha_m = 6.57\frac{V + 20.4}{1 - e^{-\frac{V+20.4}{10.3}}} \tag{3}$$

$$\beta_m = -0.304\frac{V + 25.7}{1 - e^{\frac{V+25.7}{9.16}}} \tag{4}$$

$$\alpha_h = -0.34\frac{V + 114}{1 - e^{\frac{V+114}{11}}} \tag{5}$$

$$\beta_h = \frac{12.6}{1+e^{-\frac{V+31.8}{13.4}}}. \tag{6}$$

The persistent sodium current $i_{Na}^{\text{persistent}}$ is given by:

bioRxiv preprint doi: https://doi.org/10.1101/726760; this version posted August 6, 2019. The copyright holder for this preprint (which was not certified by peer review) is the author/funder, who has granted bioRxiv a license to display the preprint in perpetuity. It is made available under aCC-BY-NC-ND 4.0 International license.

$$i_{Na}^{\text{persistent}} = g_{Nap}\, p^3\, (V - E_{Na}) \tag{7}$$

with:

$$\alpha_p = 0.0353 \frac{V + 27}{1 - e^{-\frac{V+27}{10.2}}} \tag{8}$$

$$\beta_p = -0.000883 \frac{V+34}{1-e^{(V+34)/10)}}. \tag{9}$$

The slow potassium current i_K^{slow} is given by:

$$i_K^{\text{slow}} = g_K\, s\, (V - E_K) \tag{10}$$

with $E_K = -90\text{mV}$ the reversal potential for potassium ions and:

$$\alpha_s = \frac{0.3}{1 + e^{-\frac{V+53}{5}}} \tag{11}$$

$$\beta_s = \frac{0.03}{1+e^{-(V+90)}}. \tag{12}$$

Finally, all membranes contain a leak current given by:

$$i_L = g_L\, (V - E_L). \tag{13}$$

The Q10 for gates *m*, *h*, *p* and *s* are 2.2, 2.9, 2.2 and 3.0 respectively, described at 36°C [note that this has the effect of slowing down the kinetics of gates *m*, *h* and *p* with respect to McIntyre *et al.* (25)]. All the other parameters of the model are given in **Table S1** below. Numerical values were chosen to match those observed in experiments or adapted from (20). Myelin thickness was automatically calculated using:

$$\text{Myelin thickness} = (d/g - d - 2\, psw)/2 \tag{14}$$

with d the axon diameter, g the g-ratio and psw the periaxonal space width. Myelin lamella periodicity was taken as myelin thickness divided by 6.5 so that the number of wraps is 7 in all

bioRxiv preprint doi: https://doi.org/10.1101/726760; this version posted August 6, 2019. The copyright holder for this preprint (which was not certified by peer review) is the author/funder, who has granted bioRxiv a license to display the preprint in perpetuity. It is made available under aCC-BY-NC-ND 4.0 International license.

conditions, assuming that the extracellular space between myelin lamellae comprises part of the periodicity and to account for the fact that there is no extracellular space contributing to the total width of the myelin on the most external lamella. Unless stated otherwise, simulations were run using a time step of 0.1µs and 51 nodes. Internode segments were chosen to be <1µm (0.98µm; N = 52 segments per internode) and we verified that this was sufficient to reach convergence for the conduction velocity over the whole range of simulated axons (**Figure S7**). Action potentials were triggered by a square pulse of 0.5nA lasting 10µs. The periaxonal space width was taken to be constant throughout the length of internodes. Ion channels at juxtaparanodes were not modelled, as is common in the field. When altering the length of the node of Ranvier (see below), the density of ion channels at the node was taken to be constant [see (20) for a systematic discussion of how this affects action potential conduction velocity].

To evaluate individually the effect of a node length reduction or the myelin sheath alterations on conduction velocity, we initially ran four sets of simulations. First, we used a parameter set matching the observations obtained in the sham condition (column 'Sham' in **Table S1**). We then ran the same simulations after reducing node lengths ('Short nodes'). Third, we ran simulations modifying the myelin sheath but keeping node length as per the sham condition ('Alt. myelin'). Finally, we ran a simulation with a fourth set of parameters implementing all the experimental changes observed following iTBS, i.e. a reduction in node length and alterations in the myelin sheath ('iTBS'). Simulations were run at 21°C and at 37°C (**Figure S6**).

To evaluate the functional consequence of myelin alterations, we additionally ran a set of simulations varying the periaxonal space width from 0 to 20nm at both 21°C and 37°C (**Figure S6E, F**). These simulations show that at 37°C, the periaxonal space can tune action potential conduction velocity between 4.36m/s (psw = 0nm) and 1.25m/s (psw = 20nm; **Figure S6E**). These

bioRxiv preprint doi: https://doi.org/10.1101/726760; this version posted August 6, 2019. The copyright holder for this preprint (which was not certified by peer review) is the author/funder, who has granted bioRxiv a license to display the preprint in perpetuity. It is made available under aCC-BY-NC-ND 4.0 International license.

numbers illustrate how potent and elegant this mechanism is, as it can speed up or slow down action potential conduction by a factor of 3.5 by making minor adjustments to the structure of myelinated axons. The functional consequences of this change to propagation speed at 37°C is to alter the arrival time of action potentials by 6ms over a distance of 1cm (**Figure S6F**), enough to alter learning via spike-timing dependent plasticity for instance.

Compound action potential recordings

Compound action potential (CAP) recording and conduction-velocity measurement procedures were adapted from (26). Briefly, the day after stimulation was complete, sham or iTBS-treated mice were killed by cervical dislocation and their brains rapidly dissected into ice-cold sucrose solution containing: 75 mM sucrose, 87 mM NaCl, 2.5 mM KCl, 1.25 mM NaH_2PO_4, 25 mM $NaHCO_3$, 7 mM $MgCl_2$, and 0.95 mM $CaCl_2$. Coronal vibratome sections (400 µm; 2-3 per animal spanning Bregma +0.8 and -0.2) were generated using a Leica VT1200s vibratome and incubated at ~32°C for 45 min in artificial cerebral spinal fluid (ACSF) containing 119 mM NaCl, 1.6 mM KCl, 1 mM NaH_2PO4, 26.2 mM $NaHCO_3$, 1.4 mM $MgCl_2$, 2.4 mM $CaCl_2$ and 11 mM glucose (300 ± 5 mOsm / kg), before being transferred to ~21°C ACSF saturated with 95% O_2 / 5% CO_2.

CAPs were evoked by constant current, stimulus-isolated, square wave pulses (200 ms duration, delivered at 0.2 Hz), using a tungsten bipolar matrix stimulating electrode (FHC; MX21AEW), and detected using glass recording electrodes (1-3 MΩ) filled with 3M NaCl. To quantify CAP amplitude, the asymptotic maximum for the short-latency negative peak (myelinated peak, M; **Figure 5**) was first determined by placing the stimulating and recording electrodes 1mm apart and varying the intensity of stimulus pulses (0.3–4.0 mA) using an external stimulus isolator (ISO-STIM 1D) before recording at 80% maximum stimulation. To enhance the signal-to-noise ratio,

bioRxiv preprint doi: https://doi.org/10.1101/726760; this version posted August 6, 2019. The copyright holder for this preprint (which was not certified by peer review) is the author/funder, who has granted bioRxiv a license to display the preprint in perpetuity. It is made available under aCC-BY-NC-ND 4.0 International license.

all quantitative electrophysiological analyses were conducted on waveforms that were the average of eight successive sweeps, amplified and filtered (10 kHz low pass bessel) using an Axopatch 200B amplifier (Molecular Devices), digitized at 100 kHz and stored on disk for offline analysis.

The conduction velocity of myelinated (M) and unmyelinated (UM) axons in the CC was estimated by changing the distance between the stimulating and recording electrodes from 1 to 3 mm, while holding the stimulus intensity constant (80% maximum). The peak latency of the M and UM axons was measured at each point and graphed relative to the distance separating the electrodes. A linear regression analysis was then performed to yield a slope that is the inverse of the velocity for each brain slice. The average velocity for both CAP components (M, UM) was then determined for each animal (n=7 per group) and this value was used for statistical comparison.

Statistical analyses

The number of mice analyzed in each group (*n*) or the number of cells, axons, nodes or internodes is indicated in the corresponding figure legends. Data presented for n=mice are expressed as the mean ± SD and data presented for n=cells, axons, nodes or internodes are expressed as the mean ± SEM. All statistical analyses were performed using Prism 6 (GraphPad Software). All data were first assessed using the Shapiro-Wilk ($n > 5$) or Kolmogorov-Smirnov ($n \leq 5$) normality tests and were further analysed by parametric or nonparametric tests as appropriate. Data comparing two groups at a single time point were analyzed using a parametric two-tailed t-test or a non-parametric Mann-Whitney U (MWU) test. Distribution data were analyzed using a Kolmogorov–Smirnov (KS) test. Cell counts for lineage tracing were analyzed using a 2-way ANOVA with Bonferroni post-test. Learning in the RAM was analyzed using a repeated measures one-way

bioRxiv preprint doi: https://doi.org/10.1101/726760; this version posted August 6, 2019. The copyright holder for this preprint (which was not certified by peer review) is the author/funder, who has granted bioRxiv a license to display the preprint in perpetuity. It is made available under aCC-BY-NC-ND 4.0 International license.

ANOVA with a Geisser-Greenhouse correction to ensure equal variability and sphericity was not assumed, followed by a Bonferroni post-test. ANOVA main effects are given in the corresponding figure legends.

bioRxiv preprint doi: https://doi.org/10.1101/726760; this version posted August 6, 2019. The copyright holder for this preprint (which was not certified by peer review) is the author/funder, who has granted bioRxiv a license to display the preprint in perpetuity. It is made available under aCC-BY-NC-ND 4.0 International license.

Supplementary Figures:

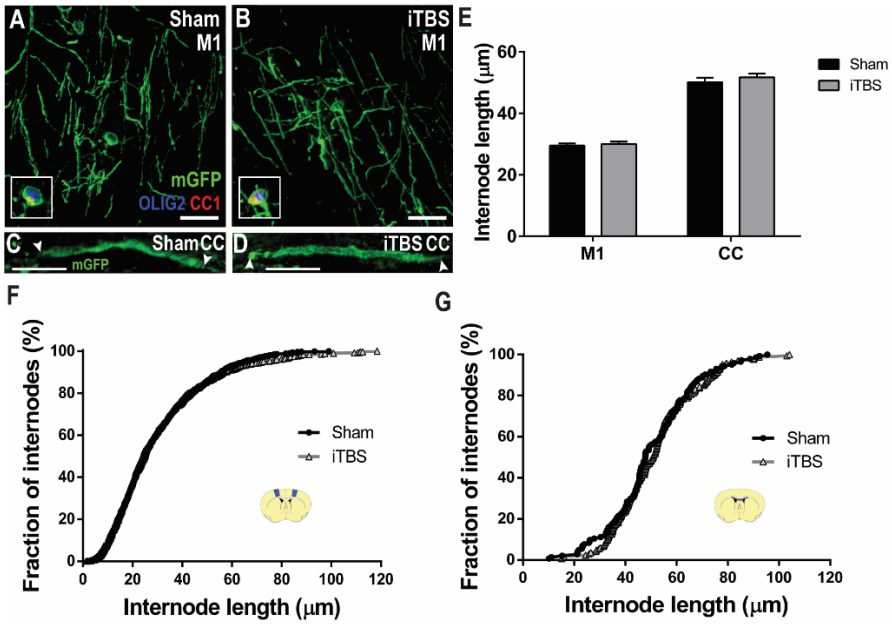

Figure S1. iTBS does not alter oligodendrocyte gross myelinating morphology
(**A-B**) Compressed confocal z-stack of a mGFP$^+$ (green) oligodendrocyte in the primary motor cortex (M1) of a *Plp-CreER::Tau-mGFP* transgenic mouse that received 14 days of sham-stimulation (**A**) or iTBS (**B**). Inset, mGFP$^+$ cell bodies show co-labeling for CC1 (red) and OLIG2 (blue). (**C-D**) Confocal image of a single mGFP$^+$ internode in the corpus callosum (CC) of a sham-stimulated (**C**) or iTBS (**D**) mouse. (**E**) Quantification of average internode length in M1 and the CC of *PlpCreER::Tau-mGFP* mice that received 14 days if sham stimulation or iTBS. (**F-G**) Graphical representation of internode length distribution for internodes supported by oligodendrocytes born and myelinating prior to receiving 14 days of sham (black) or iTBS (gray) treatment within M1 (**F**; n=744 sham and n=733 iTBS; K-S test, K-S D=0.049, p=0.32) and the CC (**G**; n=144 sham and n=166 iTBS internodes; K-S test, K-S D=0.08, p=0.63). Arrowheads indicate the end of an internode. Mean ± SEM. Oligodendrocytes sampled from n=4 animals per group. Scale bars represent 20µm.

bioRxiv preprint doi: https://doi.org/10.1101/726760; this version posted August 6, 2019. The copyright holder for this preprint (which was not certified by peer review) is the author/funder, who has granted bioRxiv a license to display the preprint in perpetuity. It is made available under aCC-BY-NC-ND 4.0 International license.

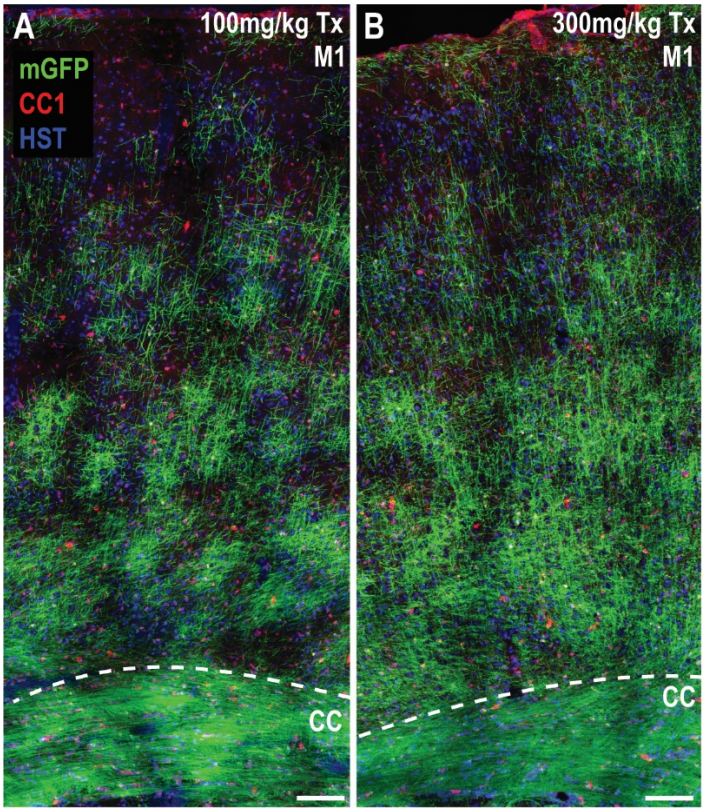

Figure S2. Mature, myelinating oligodendrocytes become mGFP-labeled following Tamoxifen administration to *PlpCreER :: Tau-mGFP* transgenic mice

(**A**) Confocal image of M1 and the CC of a P80+15 *Plp-CreER :: Tau-mGFP* mouse that received a single 100mg/kg dose of Tamoxifen (Tx), with its brain subsequently being stained to detect GFP (green), the oligodendrocyte marker CC1 (red) and Hoescht 33342 (blue). (**B**) Confocal image of M1 and the CC of a P80+15 *Plp-CreER :: Tau-mGFP* mouse that received a single 300mg/kg dose of Tamoxifen, with its brain being stained to detect GFP (green), CC1 (red) and Hoescht 33342 (blue). In mice that received only 100mg/kg of Tamoxifen, it was possible to discern individual GFP-labeled $CC1^+$ oligodendrocytes and their associated myelin internodes in the cortical layers. It was not possible to distinguish individual GFP-labeled $CC1^+$ oligodendrocytes and their associated internodes within the CC of *PlpCreER ::Tau-mGFP* mice that received 100 or 300 mg/kg Tamoxifen. Scale bars represent 100µm.

bioRxiv preprint doi: https://doi.org/10.1101/726760; this version posted August 6, 2019. The copyright holder for this preprint (which was not certified by peer review) is the author/funder, who has granted bioRxiv a license to display the preprint in perpetuity. It is made available under aCC-BY-NC-ND 4.0 International license.

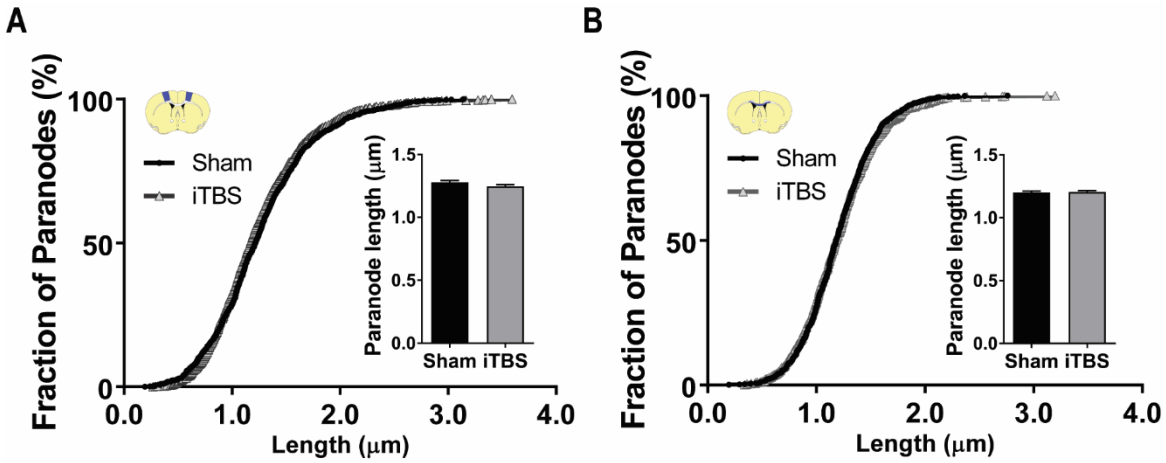

Figure S3. iTBS does not alter paranode length.
(**A**) Graphical representation of paranode length distribution in M1 (n=1268 sham and n=1335 iTBS; K-S test, K-S D= 0.052,p=0.053; Inset, quantification of average paranode length, MWU test p=0.06) (**B**) Graphical representation of paranode length distribution in the CC (n=1099 sham and n=1181 iTBS; K-S test, K-S D=0.03, p=0.65; Inset, quantification of average paranode length, MWU test p=0.73) [of mice receiving sham-stimulation (black bars) and iTBS (gray bars)]. Mean ± SEM. Paranodes sampled from n=3 animals per group.

bioRxiv preprint doi: https://doi.org/10.1101/726760; this version posted August 6, 2019. The copyright holder for this preprint (which was not certified by peer review) is the author/funder, who has granted bioRxiv a license to display the preprint in perpetuity. It is made available under aCC-BY-NC-ND 4.0 International license.

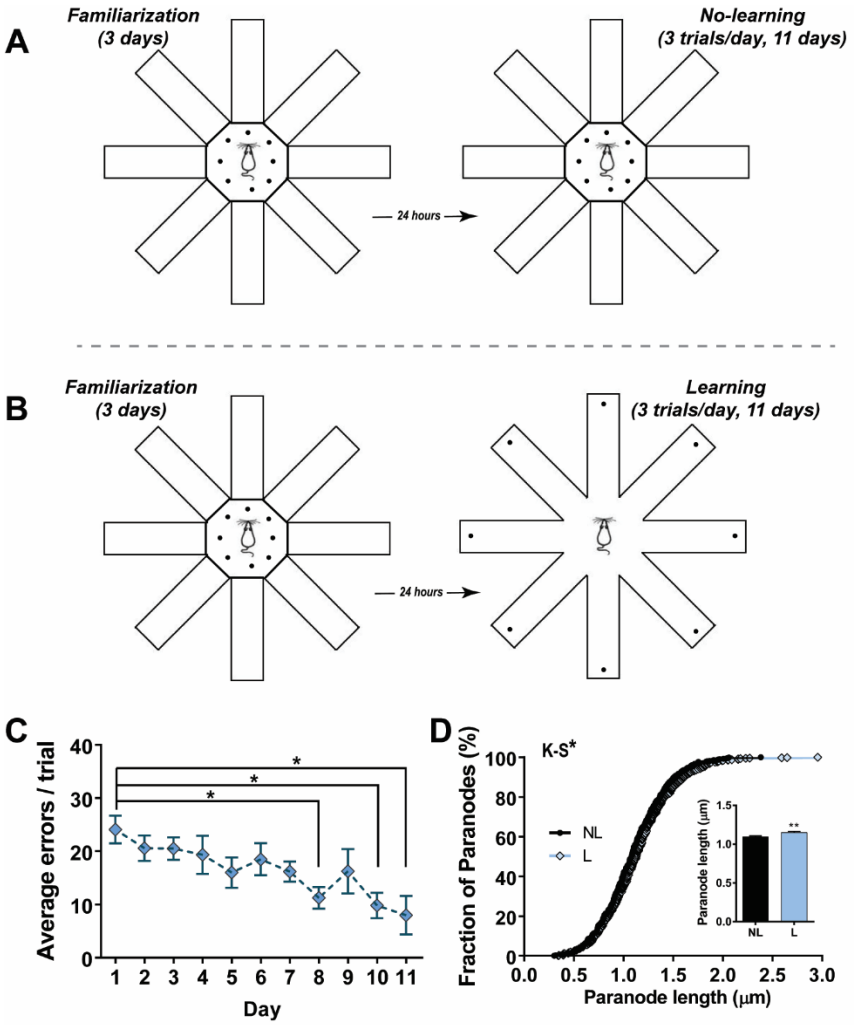

Figure S4. Spatial learning produces a very small increase in paranode length.
(**A**) Schematic outlining the radial arm maze (RAM) procedure during the first 3 days of familiarization to the maze and over the following 11 days for no-learning control mice. Each dot represents a piece of Froot Loop® that was used as a food reward stimulus and placed in the center of the maze for each trial over a total of 14 days. (**B**) Schematic outlining the procedure during the familarization phase (first 3 days) and learning phase (last 11 days) of the RAM spatial learning task. Each dot represents a piece of Froot Loop® that was used as a food reward stimulus. Food rewards were placed in the center of the maze during the familiarization phase, but a single piece of Froot Loop® was placed at the end of each arm during each trial of the learning phase. Mice learned to enter each arm and consume the single food reward only once during a trial, with repeated entries into an arm in which the food reward was already consumed being recorded as a recall error. (**C**) Quantification of the average number of errors made across 3 trials each day by mice learning the RAM task. Over the course of 11 days the mice progressively learned the task and made fewer errors. RM one-way ANOVA $F(1.84, 5.521) = 5.62$, $p=0.048$, Bonferroni post-test. Mean ± SEM for n=4 mice. (**D**) Graphical representation of paranode length distribution in the fimbria of mice that underwent no-learning (NL; black bars) or learning (L; blue bars) in the RAM task **(**n=682 no-learning and n=724 learning paranodes; K-S test, K-S D= 0.081, p=0.019; Inset, quantification of average paranode length, MWU test p=0.007). *p<0.05

bioRxiv preprint doi: https://doi.org/10.1101/726760; this version posted August 6, 2019. The copyright holder for this preprint (which was not certified by peer review) is the author/funder, who has granted bioRxiv a license to display the preprint in perpetuity. It is made available under aCC-BY-NC-ND 4.0 International license.

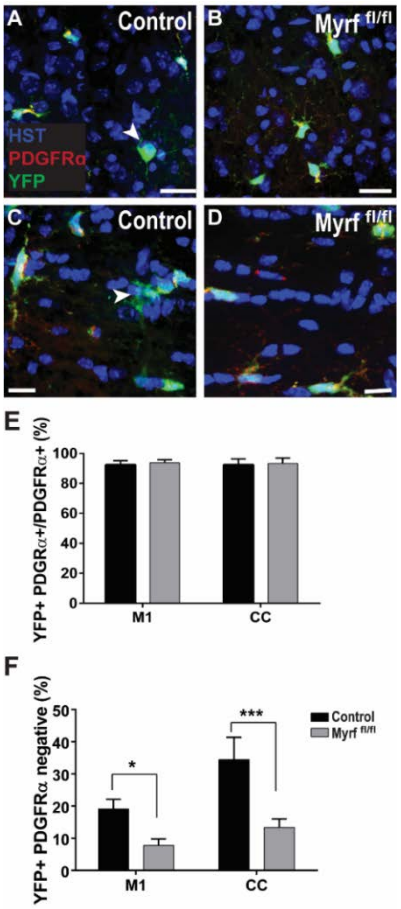

Figure S5. The conditional deletion of *Myrf* from adult mouse oligodendrocyte precursor cells reduces oligodendrogenesis

Tamoxifen was administered to P60 control (*Pdgfrα-CreER^{TM}:: Rosa26-YFP*) and Myrf$^{fl/fl}$ (*Pdgfrα-CreER^{TM} :: Rosa26-YFP :: Myrf$^{fl/fl}$*) mice to turn on expression of YFP in oligodendrocyte precursor cells (OPCs) and allow the lineage tracing of their progeny. Tamoxifen also resulted in the conditional deletion of *Myrf* from adult OPCs. (**A**) Compressed confocal image from M1 of P60+30 control mice stained to detect PDGFRα (red), YFP (green) and Hoescht 33342 (blue). (**B**) Compressed confocal image from M1 of P60+30 Myrf$^{fl/fl}$ mice stained to detect PDGFRα (red), YFP (green) and Hoescht 33342 (blue). (**C**) Compressed confocal image from the CC of P60+30 control mice stained to detect PDGFRα (red), YFP (green) and Hoescht 33342 (blue). (**D**) Compressed confocal image from the CC of P60+30 Myrf$^{fl/fl}$ mice stained to detect PDGFRα (red), YFP (green) and Hoescht 33342 (blue). (**E**) The proportion of PDGFRα+ OPCs that underwent recombination and become YFP-labeled in M1 and the CC of P60+30 control and Myrf-deleted mice (2-way ANOVA: region $F(1,39)=0.069$, $p=0.79$, gene $F(1,39)=1.62$, $p=0.21$, interaction $F(1,39)=0.08$, $p=0.76$). Mean ± SD. n=10-12 mice per group. (**F**) Quantification of the proportion of YFP-labeled (and OLIG2^{+}) cells that downregulated PDGFRα to become newly differentiated oligodendrocytes in M1 and the CC of P60+30 control and Myrf-deleted mice (2-way ANOVA: region $F(1,9)=21.93$, $p=0.001$, gene $F(1,9)=52.68$, $p<0.0001$, interaction $F(1,39)=4.70$, $p=0.058$). Arrows indicate newborn oligodendrocytes. Scale bars represent 13µm. Mean ± SD. n=3-4 mice per group. 2-way ANOVA with Bonferroni post-test *$p<0.05$, ***$p<0.001$.

bioRxiv preprint doi: https://doi.org/10.1101/726760; this version posted August 6, 2019. The copyright holder for this preprint (which was not certified by peer review) is the author/funder, who has granted bioRxiv a license to display the preprint in perpetuity. It is made available under aCC-BY-NC-ND 4.0 International license.

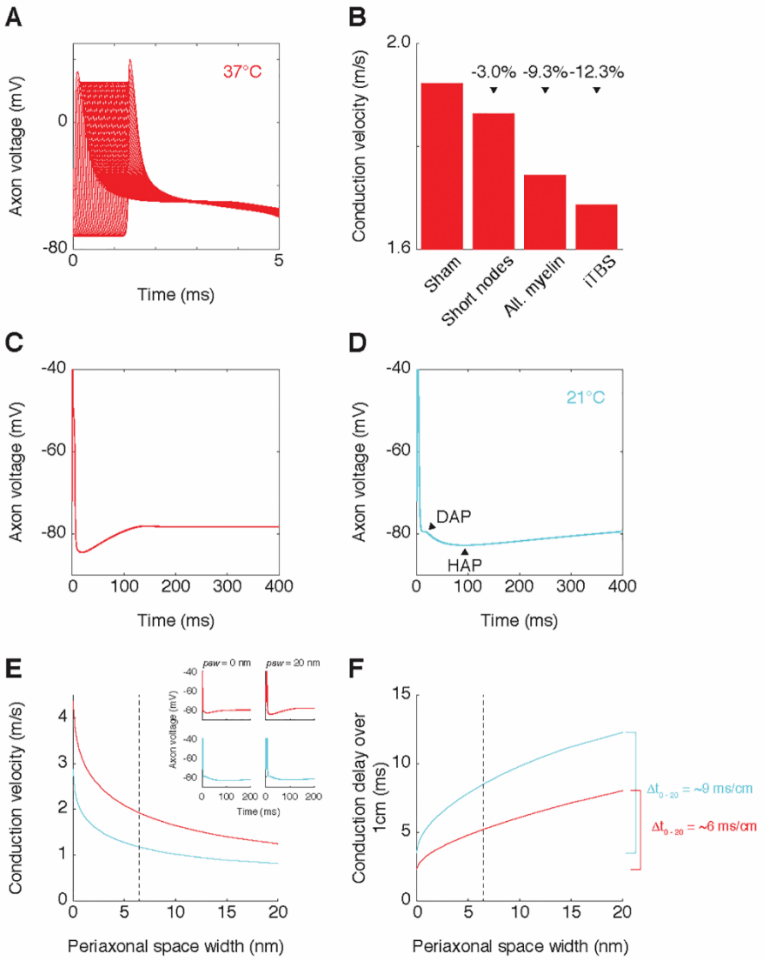

Figure S6. Mathematical simulation of conduction in myelinated central nervous system axons

(A) Action potentials simulated at consecutive nodes at 37°C. (**B**) Conduction velocity (CV) in the model at 37°C. Consistent with CV simulations at 21°C (**Figure 4**), the iTBS-induced reduction in node length produced a slight reduction in CV, while the iTBS-induced change in myelin structure (g-ratio and periaxonal space) produced a larger reduction in CV. When both modifications were simulated, their effect was additive, and reduced CV by 12.3%. (**C**) The long-term time course of action potentials generated by the model at 37°C. (**D**) The long-term time course of action potentials generated by the model at 21°C, highlighting two after-potential features; a slight depolarizing after-potential (DAP) and a hyperpolarizing after-potential (HAP), that matched those from axonal recordings of intramuscular myelinated rat axons made at room-temperature (27). For simulations in **C** and **D**, the time step was changed to 2µs. (**E**) Modification of the periaxonal space width is a very effective mechanism for adjusting CV, as it changes CV by a factor of 3.5 (from 20 to 0 nm) when simulated at 21°C (cyan) or 37°C (red) for a constant myelinated axon volume. The iTBS-altered periaxonal space width is indicated by the vertical dashed line. Insets show the action potential waveform at the two extremities of the tested range (*psw* = 0nm and *psw* = 20nm) at 21°C (cyan) or 37°C (red). (**F**) Conduction delay over 1 cm when varying the periaxonal space width between 0 and 20 nm, simulated at 21°C (cyan) or 37°C (red).

bioRxiv preprint doi: https://doi.org/10.1101/726760; this version posted August 6, 2019. The copyright holder for this preprint (which was not certified by peer review) is the author/funder, who has granted bioRxiv a license to display the preprint in perpetuity. It is made available under aCC-BY-NC-ND 4.0 International license.

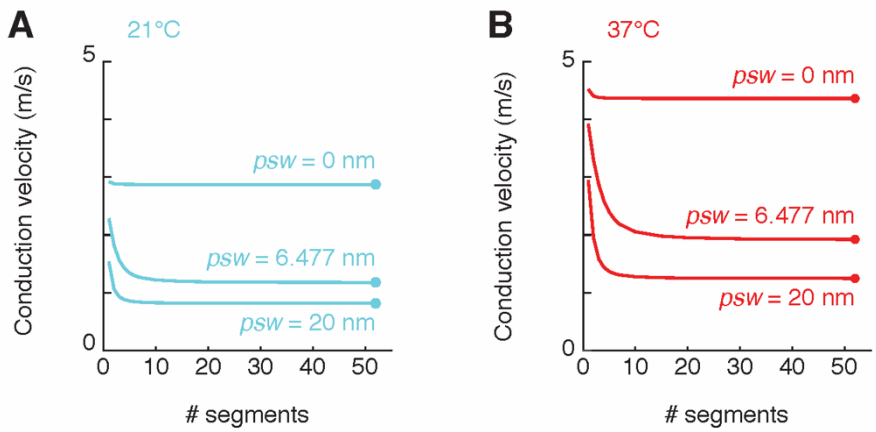

Figure S7. Controls for the convergence of conduction velocity in mathematical simulations

Conduction velocity simulations were run at 21°C (**A**) or 37°C (**B**), inputting a periaxonal space width (*psw*) within the physiological range measured in the study (6.477nm) or at two extremes (*psw* = 0nm and *psw* = 20nm), and used an increasing number of segments per internode. In all scenarios, using N = 52 segments (finishing dots), ensured that a stable prediction of the conduction velocity was reached irrespective of the width of the periaxonal space.

bioRxiv preprint doi: https://doi.org/10.1101/726760; this version posted August 6, 2019. The copyright holder for this preprint (which was not certified by peer review) is the author/funder, who has granted bioRxiv a license to display the preprint in perpetuity. It is made available under aCC-BY-NC-ND 4.0 International license.

Table S1. Parameters used in computational simulations of action potentials conduction velocity.

Parameter		**Sham**	**Short nodes ***	**Alt. myelin ***	**iTBS ***
Internode length	µm	50.32			
Axon diameter	µm	0.5894			
Node length	µm	0.8364	0.7735		0.7735
RMP	mV	-72			
Node capacitance	µF/cm^2	0.9			
Internode capacitance	µF/cm^2	0.9			
Internode leak conductance (g_L)	mS/mm^2	0.1			
E_L	mV	-84			
Axoplasmic resistivity	Ω•m	0.7			
Periaxonal resistivity	Ω•m	0.7			
Periaxonal space width	nm	6.477		8.487	8.487
g-ratio		0.724		0.6888	0.6888
Number lamellae		7			
Myelin membrane capacitance	µF/cm^2	0.9			
Myelin membrane conductance	mS/mm^2	1			
g_{Naf}	mS/mm^2	50			
g_{Nap}	mS/mm^2	0.05			
g_K	mS/mm^2	0.8			

* Only detailed if different from the sham condition.